ACS Catalysis

Research Article

pubs.acs.org/acscatalysis

Promoted Ceria: A Structural, Catalytic, and Computational Study

Ramzi Farra,[†] Max García-Melchor,[‡] Maik Eichelbaum,[†] Maike Hashagen,[†] Wiebke Frandsen,[†] Jasmin Allan,[†] Frank Girgsdies,[†] László Szentmiklósi,[§] Núria López,[‡] and Detre Teschner*[,†]

[†]Fritz-Haber-Institut der Max-Planck Gesellschaft, Faradayweg 4-6, D-14195 Berlin, Germany

[‡]Institute of Chemical Research of Catalonia, Av. Països Catalans, 16, 43007 Tarragona, Spain

[§]Centre for Energy Research, Hungarian Academy of Sciences, Budapest H-1525, Hungary

Supporting Information

ABSTRACT: The role of trivalent (La, Sm, Gd, and Y) and tetravalent (Hf, Zr, and Ti) dopants in the catalytic, structural, and electronic properties of ceria was investigated. Promoted ceria catalysts were synthesized by coprecipitation with ammonia and tested in HCl and CO oxidation. Ceria catalysts exhibit a medium high reactivity and excellent stability in HCl oxidation. The intrinsic reactivity of ceria in HCl oxidation can be improved by a factor of 2 when doping with Hf and Zr in appropriate quantities, whereas trivalent dopants are detrimental. Although both oxidation reactions rely on the existence of oxygen vacancies, the order of reactivity in HCl and CO oxidation is not completely parallel. The effects of promoters on the electronic conductivity and the vacancy formation energy were studied by contactless conductivity experiments using the microwave cavity perturbation technique and by density functional theory calculations. Furthermore, transport properties were also assessed on the basis of theoretical calculations. The order of oxygen vacancy formation energy follows well the order of conductivity (polaron mobility) (trivalent > tetravalent > undoped) observed under inert and oxidizing conditions. This implies that none of these properties correlates with the reactivity. On the other hand, reducing conditions strongly enhanced the conductivity of Hf- and Zr-doped ceria. In HCl oxidation, only the balanced reduction of both Cl and O vacancy formation energies allows for an enhanced reactivity. Promoters give rise to lattice contraction−expansion modifying vacancy formation energies, adsorption properties, and surface coverages.

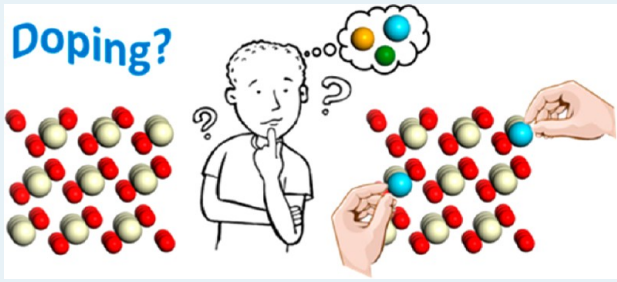

KEYWORDS: *CeO_2, dopants, conductivity, XRD, PGAA, DFT, HCl oxidation, Deacon Reaction, CO oxidation*

INTRODUCTION

Ceria is widely utilized in various catalytic processes as a support, as an additive, and as the active phase of the reaction. However, even when used as a support, it is not merely an inactive carrier. Because of the relative ease with which ceria can be reduced and the mobility of its lattice oxygen ions, it is an efficient material in redox reactions. Hence, ceria is a key component as an oxygen ion-conducting solid electrolyte in solid oxide fuel cells[1,2] and in automotive exhaust catalysis.[3] Further, it can be applied in SO_2 oxidation,[4,5] in Diesel soot oxidation,[6] in water-gas shift (WGS)[7,8] and preferential oxidation of CO (PROX)[9,10] reactions, in oxidative halogenations,[11] and in HCl oxidation.[12,13]

In most of these reactions, the facile formation and annihilation of oxygen vacancies and reduced ceria sites likely play a crucial role. It is typically believed that in catalytic oxidations using ceria, the molecule to be oxidized takes oxygen from the oxide lattice, thereby creating oxygen vacancies on the surface. Reactant oxygen from the gas phase can subsequently replenish the vacancy and reoxidize the Ce^{3+} sites. Because this process of filling vacancies by oxygen is exothermic, particular attention has been focused on vacancy formation.[14−20] The local structure of surface and subsurface oxygen vacancies and vacancy clusters was revealed by scanning tunneling microscopy,[14] while density functional theory (DFT) calculations suggested that the vacancy formation energy is structure sensitive[15−17] and that metals present as dopants[21−25] or adsorbed on top affect this parameter.[26] The most stable $CeO_2(111)$ surface has a comparatively high vacancy formation energy (1.9−2.7 eV), whereas removal of oxygen from facets with a higher surface energy, e.g., (110), (100), and (310), is easier. Vacancy density was also experimentally found to be dependent on particle shape and, accordingly, the surface type exposed.[27] Consequently, surface reactions, such as CO oxidation, were also found to be structure sensitive over ceria.[28−30]

The addition of promoters (dopants) has been frequently used to improve a certain target property of ceria. For example, ionic conductivity is much enhanced by trivalent dopants such as Gd and Sm,[31] whereas reducibility and oxygen storage capacity are facilitated by the incorporation of Zr or Hf into the cubic structure.[22,32,33] Furthermore, addition of Zr improves

Received: July 3, 2013
Revised: August 23, 2013
Published: August 26, 2013

   dx.doi.org/10.1021/cs4005002 | ACS Catal. 2013, 3, 2256−2268

the structural integrity of ceria, preserving the cubic phase. Promoters also were found to enhance the reactivity of ceria in CO oxidation.[34,35] The role of Zr and La doping of Pt/CeO_2 in the WGS reaction was also recently investigated.[36,37]

Our interest in ceria stems from its medium high reactivity and excellent stability in HCl oxidation (Deacon process, eq 1).[12,13]

$$\frac{1}{2}O_2 + 2HCl \rightarrow Cl_2 + H_2O \quad (1)$$

This reaction involves reactive HCl adsorption by proton abstraction with surface lattice oxygen, the formation of surface Cl, the recombination of surface species to produce gas-phase chlorine and water, and subsequent reoxidation of the surface by dissociative oxygen activation. Therefore, adsorption and recombination steps replenish or generate surface vacancies. Most Cl species substitute surface lattice O sites, which are tightly bound Cl species. Using *in situ* surface analysis, we recently concluded that HCl oxidation is also structure sensitive and only minority sites are responsible for the reactivity.[38]

In this work, promoted ceria catalysts prepared by coprecipitation are evaluated and compared in HCl and CO oxidation. We show that in HCl oxidation the intrinsic reactivity of ceria, when using an Hf or Zr dopant in appropriate quantities, can be enhanced by a factor of ~2, whereas trivalent dopants are detrimental. Moreover, the structure, conductivity, and the surface Cl coverage of promoted samples were investigated to reveal the key physicochemical properties of these materials. Mechanistic details of promoted ceria were assessed by DFT calculations of the vacancy formation energy in removing Cl or O from the surface, as well as the vacancy and electron transport barriers for various doped ceria materials.

EXPERIMENTAL AND COMPUTATIONAL METHODS

Preparation of Catalysts. Doped ceria catalysts (Table 1) were synthesized by coprecipitation of guest and host precursors (nitrates or chlorides) from the aqueous phase with an NH_3 solution, followed by aging of the precipitate in the mother liquor and calcination after washing and drying. Controlled coprecipitation was performed in an automated laboratory reactor system (Mettler-Toledo LabMax) where the pH of 9 and the temperature (318 K) were controlled by *in situ* probes. The following precursors were used: $Ce(NO_3)_3{\cdot}6H_2O$, $La(NO_3)_3{\cdot}6H_2O$, $Sm(NO_3)_3{\cdot}6H_2O$, $Gd(NO_3)_3{\cdot}6H_2O$, $Y(NO_3)_3{\cdot}4H_2O$, $HfCl_4$, $ZrCl_4$, and $TiCl_4$. Catalysts with different doping cations and concentrations were prepared according to the following procedure: A 200 cm^3 solution of a mixture of host and guest components (0.2 M Ce^{4+} and the corresponding concentration of the guest) was dosed into a reactor filled with 400 cm^3 of bidistilled water within 25 min, while the pH value was adjusted to 9 by simultaneous addition of appropriate amounts of an ammonia solution (10 wt %). The precipitate was subsequently aged at the same temperature for 60 min while being stirred in the mother liquor. A typical LabMax protocol is shown in Figure S1 of the Supporting Information. No variation in pH was observed during the aging period. Thereafter, the precipitate was filtered, washed (three times with bidistilled water, once with ethanol, and finally with acetone), and dried. The resulting wet cake was covered and dried overnight at 373 K. The dried material was ground in a mortar to achieve better homogeneity before the calcination step. Calcination (5 K/min) was performed in flowing air (100 cm^3/min) at 973 K for 5 h.

Table 1. Samples with Their Codes, BET Surface Areas, and Cl_2 Space Time Yields under Standard Conditions

		S_{BET} (m^2/g)		
sample	sample code[a]	fresh	used in HCl oxidation	space time yield[b] (g of Cl_2 g_{cat}^{-1} h^{-1})
CeO_x	CeO_2 (14766)	55.5	47.2	2.1
$Ce_{0.95}La_{0.05}O_x$	CeLa-5 (14687)	52.0	45.1	1.4
$Ce_{0.95}Sm_{0.05}O_x$	CeSm-5 (14676)	46.9	44.9	1.6
$Ce_{0.95}Gd_{0.05}O_x$	CeGd-5 (14650)	31.1	27.9	1.2
$Ce_{0.95}Y_{0.05}O_x$	CeY-5 (14679)	45.8	39.4	1.8
$Ce_{0.95}Ti_{0.05}O_x$	CeTi-5 (16097)	36.4	30.5	2.1
$Ce_{0.99}Zr_{0.01}O_x$	CeZr-1 (15225)	34.3	48.6	2.7
$Ce_{0.975}Zr_{0.025}O_x$	CeZr-2.5 (15228)	55.6	46.2	2.6
$Ce_{0.95}Zr_{0.05}O_x$	CeZr-5 (15232)	62.3	49.0	2.8
$Ce_{0.9}Zr_{0.1}O_x$	CeZr-10 (15289)	68.4	49.4	3.0
$Ce_{0.8}Zr_{0.2}O_x$	CeZr-20 (15291)	64.1	48.3	3.0
$Ce_{0.99}Hf_{0.01}O_x$	CeHf-1 (14728)	71.8	51.7	2.0
$Ce_{0.975}Hf_{0.025}O_x$	CeHf-2.5 (14730)	87.1	55.4	2.8
$Ce_{0.95}Hf_{0.05}O_x$	CeHf-5 (14685)	64.1	53.4	3.0
$Ce_{0.9}Hf_{0.1}O_x$	CeHf-10 (14762)	90.1	49.8	3.1
$Ce_{0.8}Hf_{0.2}O_x$	CeHf-20 (14764)	39.0	41.6	2.5

[a]Internal (FHI) sample codes in parentheses. [b]Reaction conditions: 703 K, 9:1 O_2:HCl ratio, flow rate of 166 cm^3/min, catalyst weight of 0.25 g. Space time yield after 2 h on stream.

Basic Characterization. The powder X-ray diffraction (XRD) measurements were performed on a STOE STADI P transmission diffractometer equipped with a primary focusing germanium monochromator (Cu Kα_1 radiation) and a linear position sensitive detector, and on a STOE Theta/theta Bragg-Brentano diffractometer equipped with a DECTRIS MYTHEN1K one-dimensional silicon strip detector (Ni-filtered Cu radiation). XRD data were evaluated by total pattern analysis using TOPAS.[39] An empirically obtained convolution accounted for the instrumental contribution to the peak profiles, while the sample contribution was described according to the Double-Voigt approach.[40] Crystallite sizes were calculated from the $1/\cos(\theta)$ Voigt function and are given as L_{Vol}-IB values (volume-weighted mean column length based on integral breadth), i.e., without making further assumptions about crystallite shapes or size distributions, while strain contribution ε_0 was derived from the $\tan(\theta)$ Voigt component. Scanning electron microscopy (SEM) images were captured on a Hitachi S-4800 field emission scanning electron microscope at a working voltage of 1.5 kV. The microscope was equipped with an EDAX system with a Sapphire Si(Li) detecting unit, which was used for elemental analysis by energy dispersive X-ray spectroscopy (EDX). Nitrogen adsorption was conducted at 77 K on a Quantachrome Autosorb-6B analyzer. Prior to the measurement, the samples were outgassed in vacuum at 423 K for 5 h.

Contactless Conductivity Experiments Using a Microwave Cavity Perturbation Technique. The *in situ* microwave cavity perturbation technique (MCPT) setup, which was described in detail recently,[41] allows the measurement of the electrical conductivity of (powder) samples in a fixed-bed flow-through reactor at temperatures up to 773 K in various gas atmospheres with on-line probing of reactants and products for the simultaneous deduction of kinetic reaction data. More

dx.doi.org/10.1021/cs4005002 | ACS Catal. 2013, 3, 2256−2268

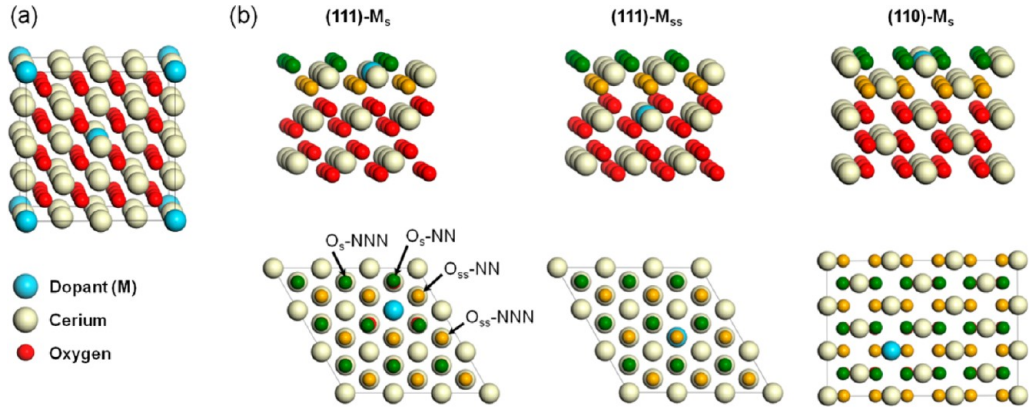

Figure 1. Side view of the M-doped CeO_2 bulk structures (a) and side and top views of the different M-doped CeO_2 (111) and (110) surfaces (b) employed for the DFT calculations.

details of the setup and data evaluation are provided in the Supporting Information. For this investigation, the 0.1−0.315 mm sieve fractions of undoped CeO_2 and CeO_2 doped with 5% Hf, Zr, La, and Sm were measured in a quartz tube reactor with a 3 mm inner diameter placed in the center of the microwave X-band cavity resonating in the TM_{110} mode at 9.2 GHz. The length of the catalyst bed was 10 mm, and a 20 cm^3/min flow of different inert, reducing, and oxidizing gas mixtures was applied. Every sample was first dehydrated in N_2 at 623 K for 30 min, then cooled to 303 K, and heated again to 623 K at a rate of 10 K/min, followed by isothermal treatments at 623 K in N_2 and H_2/N_2 and O_2/N_2 mixtures.

***In Situ* Prompt Gamma Activation Analysis (PGAA).** *In situ* PGAA was utilized to measure the uptake of Cl of (promoted) ceria during HCl oxidation. The technique is based on the detection of element-specific γ-rays emitted upon excitation of the nucleus with cold neutrons. The investigated volume, in our case a tubular quartz microreactor, was probed, and the amounts of Cl, Ce, and dopants were quantified. PGAA was conducted at the cold neutron beam of the Budapest Neutron Centre. For further details, see the Supporting Information.

Catalytic Tests. The gas-phase oxidation of hydrogen chloride was studied at ambient pressure in the same quartz microreactor that was used for the *in situ* PGAA experiment. The catalyst (sieve fraction of 0.1−0.315 mm) was loaded in the reactor (8 mm inside diameter) and pretreated in N_2 at 703 K for 30 min. Thereafter, the reaction gases were introduced at a total flow rate of 166 cm^3/min. Catalysts were tested in the temperature range of 623−703 K and at different O_2:HCl ratios. The flow of HCl was always constant at 16.6 cm^3/min, and the oxygen flow was balanced with N_2. Used samples were collected for postreaction characterization after the reactor had been rapidly cooled to room temperature in a flow of N_2. Stability testing was performed with CeHf-10 for 100 h. Cl_2 quantification and calculation of the HCl conversion were based on iodometric titration.

CO oxidation over ceria and promoted ceria samples was conducted at ambient pressure in a fixed-bed microreactor using 0.2 g of catalyst (sieve fraction of 0.1−0.25 mm). The catalyst was diluted and well-mixed with 0.4 g of SiC (sieve fraction of 0.25−0.335 mm) to minimize hot spot formation. The raction temperature was controlled by a K-type thermocouple inserted directly into the catalyst bed. The sample, loaded into a U-shaped stainless steel tube (4 mm inside diameter) with glass-lined tubing, was pretreated in flowing 5% O_2 in He (total flow of 100 cm^3/min) at 660 K for 1 h and cooled to ∼400 K in an O_2/He atmosphere. The gas was switched to the reaction mixture (1% CO and 1% O_2 in He; total flow of 100 cm^2/min) at 400 K, and the reactor was held at this temperature for 5 min for stabilization. Conversion versus temperature curves (light-off profiles) were collected by increasing the temperature at a rate of 2 K/min until the temperature reached 660 K and monitoring CO conversion. Furthermore, with CeHf-5 and CeLa-5, a cooling experiment was performed to check for deactivation or hysteresis of the reactivity. Additionally, O_2-dependent experiments were also conducted with these two samples at 550 K. A Rosemount Analytical X-STREAM on-line multicomponent gas analyzer was used for measuring the volume percentage of CO, O_2, and CO_2 in the effluent gas stream, which uses a nondispersive infrared analyzer for detecting CO and CO_2, and a paramagnetic analyzer for O_2. After each experiment, the reactor tube was cleaned with aqua regia, and a blind test was performed to ensure and verify the lack of cross contamination. The blank reactivity at the maximal temperature (660 K) was always <2% CO conversion.

Computational Details. All the calculations were carried out using the Vienna *ab initio* simulation package (VASP, version 5.3.2).[42,43] As the electronic structure of CeO_2 is a strongly correlated system, the Perdew−Burke−Ernzenhof (PBE) gradient-corrected functional[44] was employed and the self-interaction error was mitigated through the addition of a *U* Hubbard-like term following the approach of Dudarev et al.[45] The effective *U* parameter (U_{eff} = 4.5 eV) was chosen on the basis of the satisfactory results reported in previous theoretical studies.[18,46] In all the calculations, core electrons were represented by the projector-augmented wave (PAW)[47] method, with cores [Kr]$4d^{10}$, [Kr]$4d^{10}4f^{14}$, [Ar]$3d^{10}$, [Kr]$4d^{10}$, [Kr]$4d^{10}4f^5$, [He], and [Xe] for Ce, Hf, Zr, La, Sm, O, and Cl atoms, respectively, whereas the valence ones were expanded in plane waves with a cutoff energy of 500 eV. Ceria has a fluorite structure, and the calculated lattice constant (a_{calc}) obtained with a dense 7 × 7 × 7 Monkhorst−Pack[48] *k*-point mesh was 5.497 Å (a_{exp} = 5.412 Å), which is in very good agreement with previous theoretical studies.[46,49] The M-doped CeO_2 (M = Hf, Zr, La, and Sm) bulk structures with a concentration of dopant of ∼6% were modeled as 2 × 2 × 2 cubic supercells as shown in Figure 1a and fully optimized using a 3 × 3 × 3 Monkhorst−Pack *k*-point mesh. The M-doped CeO_2 catalysts employed for

dx.doi.org/10.1021/cs4005002 | *ACS Catal.* 2013, 3, 2256−2268

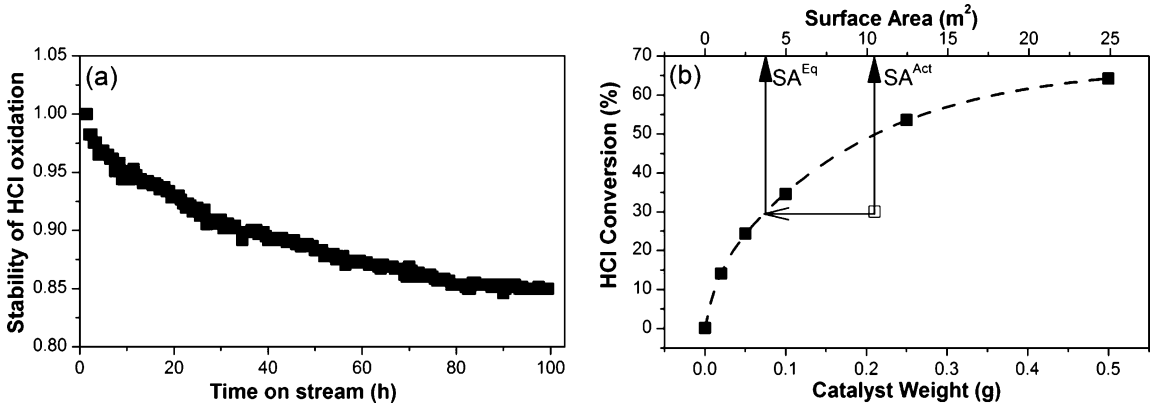

Figure 2. (a) Stability test. Normalized HCl conversion over CeHf-10 vs time on stream. Conditions: 703 K, 1:9 HCl:O_2 ratio, catalyst weight of 0.25 g. (b) HCl conversion (■) over CeHf-10 vs the reactor loading expressed in weight and surface area. Conditions: 703 K and 9:1 O_2:HCl ratio. A hypothetical other catalyst (□) is also shown. The intrinsic reactivity of the samples (i.e., the efficiency to provide a certain number of turnovers to occur) is compared on the basis of the actual surface area (SA^{Act}) of the sample and the equivalent surface area (SA^{Eq}) by SA^{Eq}/SA^{Act}. Please note that the fit shown (−−−) does not correspond to the 0.5 order power fit because of the slowly approaching equilibrium above 60% HCl conversion. Instead, a mathematically better fitting can be obtained for the whole 0−64% conversion range using an Exponential Decay 2 function (in Origin Pro), which is shown here and was used to calculate SA^{Eq}.

the study of the Deacon reaction were constructed using the optimized lattice constants of the doped bulk structures described above and considering its two lowest surface energy facets, (111) and (110) (see Figure 1b). The (111) surfaces were simulated as periodically repeated slabs of three O−Ce−O trilayers with a vacuum space of 15 Å between them. The geometry optimizations of these (111) surfaces were performed using a surface periodicity of $p(3 \times 3)$ unit cells and a $3 \times 3 \times 1$ Monkhorst−Pack mesh for the k-point sampling. During these optimizations, the five outermost layers were allowed to fully relax, whereas the four bottom layers were kept fixed in their bulk positions. On the other hand, the (110) surfaces were constructed as slabs of five layers separated with a vacuum space of 15 Å. In this case, geometries were optimized using a $p(3 \times 3)$ periodicity and a $2 \times 3 \times 1$ Monkhorst−Pack mesh and fully relaxing the top three layers. In all geometry optimizations, total energies converged better than 10^{-5} eV in the self-consistent field and the structures were relaxed with an energy threshold of 10^{-4} eV.

Spin polarization was employed when needed, and a careful analysis of the localization of the excess of charge was performed.[50] In these calculations, a ferromagnetic spin state for the localized electrons was imposed. Some test calculations (see Table S1 of the Supporting Information) showed that the difference between the ferromagnetic and antiferromagnetic spin states is very small, in agreement with previous theoretical works.[18,20,51] With this setup, the vacancy formation energy for the clean (111) surface is 2.36 eV, in good agreement with data in the literature for the same charge localization (2.22 eV).[52] Some tests regarding charge localization, geometric distortions induced, and comparison to previous calculations[18,20] can be found in the Supporting Information (Tables S2−S4). For trivalent dopants, the configuration with a M^{3+}-$O^{\bullet}$ character was investigated following the results from ref 25.

RESULTS

HCl Oxidation. Promoted and unpromoted catalysts prepared by coprecipitation were tested in HCl oxidation (Table 1). First, catalysts with a 5% dopant concentration were investigated in a standard reaction mixture (703 K and 9:1 O_2:HCl ratio). The addition of the tetravalent dopants, Zr and Hf, improved the reactivity of ceria, whereas trivalent dopants were clearly detrimental. Second, Hf- and Zr-modified catalysts with a dopant concentration in a range of 1−20% were prepared and tested in HCl oxidation. The results pointed out that 10% Hf and 10 or 20% Zr represent the optimal dopant concentration. All materials suffered slight deactivation, typically in the range of ∼3−5%, within the first 5 h on the reaction stream. To assess the long-term stability of the catalysts, we selected the best material, CeHf-10, and tested its reactivity evolution over 100 h on stream (Figure 2a). Deactivation slows over time, and the catalyst is essentially stable after 80−90 h, with an overall 15% loss of initial reactivity.

Kinetic investigations were also conducted to compare the promoted samples; the temperature dependence was explored for all catalysts, whereas selected materials were tested for pO_2 partial pressure dependence. The temperature dependence of the catalyst bed was evaluated for a 9:1 O_2:HCl reaction mixture in the range of 643−703 K. The apparent activation energy of the catalysts varies in the range of 55−78 kJ/mol, with most samples scattering around 60 kJ/mol. The highest value was observed with CeTi-5, followed by the materials with trivalent dopants. Although the range of the apparent activation energy is small, the data indicate a weak Constable−Cremer relation (compensation phenomenon),[53,54] that is, a linear correlation between the apparent activation energy and the logarithm of the apparent pre-exponential factor (Figure S3a of the Supporting Information). A similar compensation phenomenon was recently observed with a RuO_2-based HCl oxidation catalyst, by modulating the surface coverage of rate-limiting surface species.[55] The oxygen pressure dependence (Figure S3b of the Supporting Information) was measured with selected samples by varying the O_2:HCl ratio from 1 to 9 at 703 K. All investigated catalysts revealed an apparent oxygen order of ∼0.4, in line with results reported for ceria catalysts.[13,38] However, as HCl oxidation is associated with strong product inhibition,[38,56] the apparent order of 0.4 would be significantly higher (close to 1)[56] when products were co-fed into the reaction mixture to minimize the effect of varying product concentrations. Hence, O_2 activation is a critical elementary step with promoted ceria materials, as well.[12]

dx.doi.org/10.1021/cs4005002 | ACS Catal. 2013, 3, 2256−2268

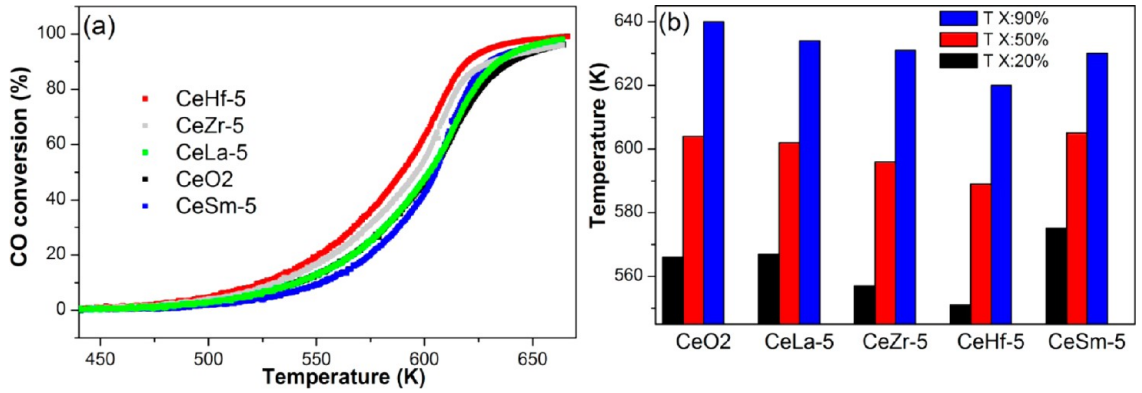

Figure 3. (a) CO oxidation light-off profiles of selected catalysts at a 1:1:98 O_2/CO/He mixture and (b) temperatures allowing 20, 50, and 90% CO conversion. Catalyst weight of 0.2 g and flow rate of 100 cm^3/min.

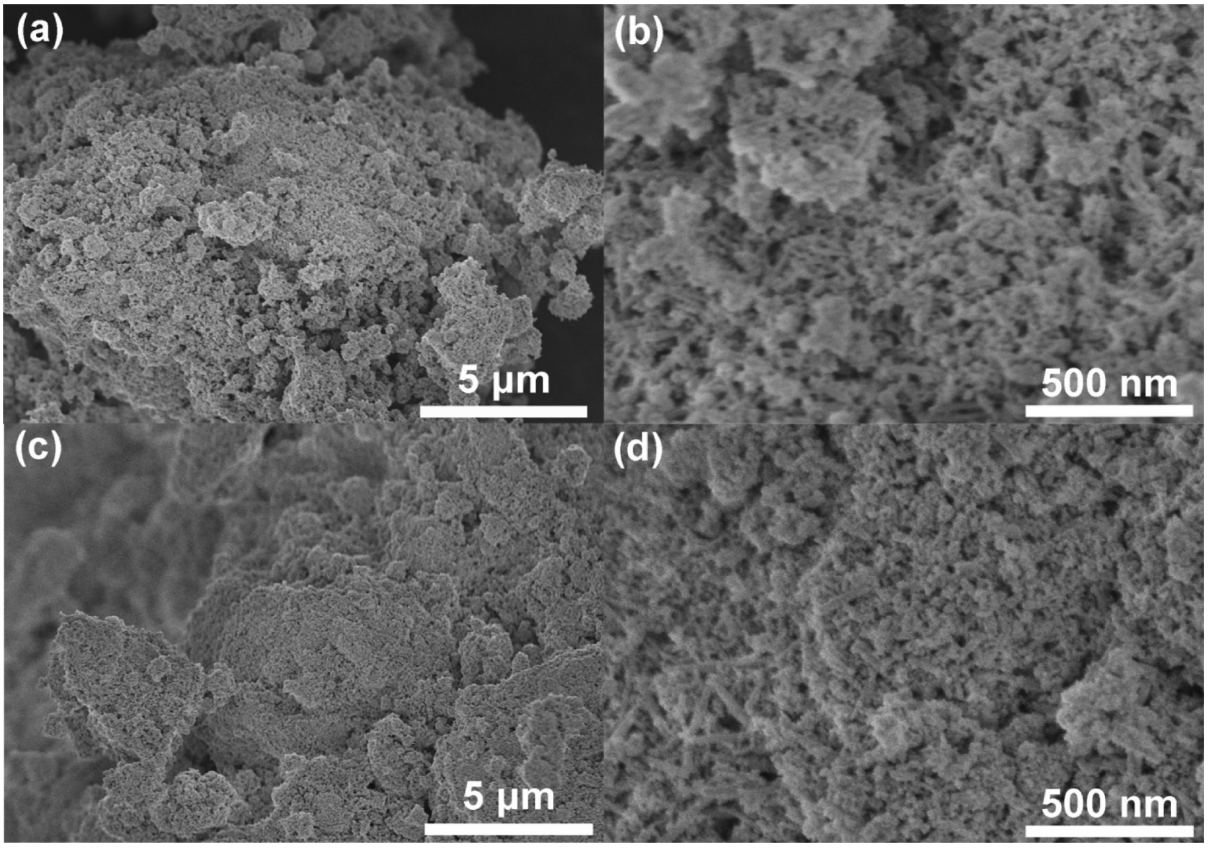

Figure 4. SEM of CeHf-10 as prepared (a and b) and after a 100 h stability test in HCl oxidation (c and d).

One unfortunate consequence of product inhibition is that the observed HCl conversion does not linearly scale with the catalyst weight used to load the reactor. This is illustrated in Figure 2b with the example of CeHf-10, where the obtained level of HCl conversion is plotted as a function of catalyst weight (and surface area) loaded into the reactor. The dependence can be best described as a 0.5 order function, typical for product inhibition when two products (Cl_2 and H_2O here) impede the reaction with an order of −1.[57] Thus, the intrinsic reactivity of catalysts cannot be estimated and compared directly by surface area normalization, and the space time yield and reaction rate values will depend on catalyst loading (total surface area). Note that all recent HCl oxidation catalysts seem to be affected by product inhibition. This was verified and discussed for RuO_2,[56] and also for ceria.[38] Here we show that the same product inhibition occurs with the best doped sample (CeHf-10), and therefore, this behavior is rather general. However, knowing the 0.5 order dependence on catalyst weight (and surface area), we can use for each catalyst the observed HCl conversion level to estimate an equivalent surface area (SA^{Eq}) of the reference CeHf-10 that gives the same HCl conversion. When comparing this equivalent surface area to the actually used one (SA^{Act}), one can estimate the efficiency and, consequently, the intrinsic reactivity of these materials in comparison to each other. Intrinsic reactivity will be further analyzed in the Discussion.

CO Oxidation. CO oxidation is a widely employed test reaction for characterizing ceria-based materials. It requires reactant adsorption, O vacancy formation, and replenishment, and thus, some elementary steps are common to HCl oxidation.

dx.doi.org/10.1021/cs4005002 | ACS Catal. 2013, 3, 2256−2268

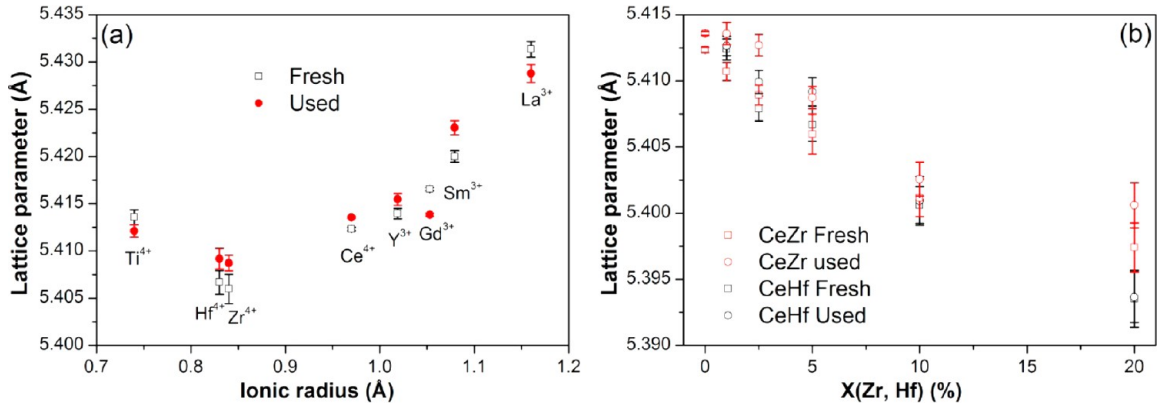

Figure 5. (a) Plot of the lattice parameter as a function of effective ionic radius of the guest ion for fresh materials and those used in HCl oxidation. The ionic radius is an effective radius of Shannon,[71] with a coordination number of 8. (b) Plot of the lattice parameter as a function of guest ion concentration of Zr and Hf. Error bars correspond to ±3 times the estimated standard uncertainties.

As HCl oxidation was enhanced by Hf and Zr promotion and inhibited by trivalent (including Sm and La) doping, we selected these four doped catalysts and the unpromoted ceria to test these materials in CO oxidation. To study the reactivity of the catalysts, we adopted the often utilized methodology of recording the light-off curves for CO oxidation. The light-off profiles for a 1:1:98 O_2/CO/He feed mixture are compiled in Figure 3a. CO conversion is essentially zero at 400 K, and the onset of reactivity is in the range of 470−520 K. Although the reactivity of the samples is not vastly different, markedly, Hf-promoted CeO_2 and Zr-promoted CeO_2 are the most reactive samples, and doping with Sm, particularly at low levels of conversion, is the least efficient. For an easier comparison, Figure 3b provides the temperatures at which the catalysts reach 20, 50, and 90% CO conversion. CeSm-5 lags ∼20 K behind CeHf-5 at lower levels of conversion, while the reactivity of CeSm-5 rapidly improves above 600 K. CeO_2 and CeLa-5 are equally active up to ∼590 K, while at higher temperatures, CeLa-5 is slightly more reactive. Above 55% conversion, the undoped ceria was the least reactive sample. The apparent activation energy (evaluated from the smooth conversion range of ∼5−40%) was calculated to be between 64 and 86 kJ/mol (Figure S4 of the Supporting Information); the lowest value was found with CeHf-5 and the highest with CeSm-5. Interestingly, the Arrhenius plot of CeSm-5 (Figure S4a of the Supporting Information) reveals an increase in the slope at ∼560−570 K (near 15% CO conversion), suggesting a change in surface state likely due to surface segregation. A similar but slightly less pronounced effect was found with CeLa-5 (not shown). Despite the narrow range of apparent activation energies, the values fit to a compensation plot (Figure S4b of the Supporting Information). Repeated light-off experiments were performed with CeHf-5 and CeLa-5 (as an example of +4 and +3 promoted samples, respectively), and the sample was subsequently cooled to see how the reactivity evolves during cooling. The CO conversions in the heating and cooling sections almost perfectly overlap for CeHf-5 (Figure S4c of the Supporting Information), whereas there is a slight activation for CeLa-5; that is, the latter shows slightly higher CO conversion in the cooling experiment. Furthermore, after the samples had been cooled to 550 K, we varied the O_2 content (1, 2, 5, and 10% vs 1% CO) of the reaction feed. The results indicate a very minor dependence on O_2, the formal reaction order of O_2 being 0.07 for CeHf-5 and 0.11 for CeLa-5 (Figure S4d of the Supporting Information).

Structural Characterization of Promoted Ceria. The BET surface areas of all catalysts in their as-synthesized form as well as after HCl oxidation are listed in Table 1. The BET values range from 31 to 90 m^2/g, typically around 45−65 m^2/g, and after HCl oxidation, most catalysts undergo a slight loss of surface area. The morphology of selected samples was investigated by SEM and is exemplified in Figure 4. SEM revealed that the primary nanoparticles (<50 nm) agglomerated into much larger secondary particles, forming a porous structure. Although the shape of nanoparticles is irregular and often not discernible, it is worth mentioning that several nanoparticles possess an elongated, needlelike structure. The morphology seems to be conserved after HCl oxidation (100 h stability test with CeHf-10). EDX experiments were conducted with the Hf-doped catalysts to estimate the amount of Hf introduced into the structure. The analysis confirmed that the nominal Hf concentration was reached in these materials; moreover, after a 100 h stability test with CeHf-10, the same ∼10% Hf concentration was observed, indicating that the dopant was not leached and removed upon HCl oxidation. PGAA experiments (under HCl oxidation, *vide infra*) assessed the promoter concentration of selected catalysts and confirmed that the nominal concentration of dopants was established during preparation.

The XRD pattern of the unpromoted CeO_2 suggests the sole presence of face-centered cubic fluorite structure (lattice constant a = 5.412 Å). Upon introduction of 5% dopant into the ceria, the materials remain single-phase and consequently accommodate the strain caused by the modified size of the dopant cations. The lattice parameter of the 5% dopant samples correlates approximately with the ionic radius of the guest ion considering an 8-fold coordination given by the host structure (Figure 5a); the larger trivalent cations expand the lattice, whereas contraction occurs with Hf and Zr dopants. CeTi-5 gives rise to deviation from this trend, as its lattice parameter (a = 5.413 Å) is significantly larger than expected from the size of the Ti^{4+} cation. Although no second crystalline phase could be identified with CeTi-5 either, the deviation indicates that the difference in the ionic radii of Ce and Ti could not be accommodated by decreasing the lattice parameter, and rather phase separation or segregation occurred. If amorphous, the Ti-rich phase would be invisible in XRD analysis. As the performance of the catalyst was not exceptional, we have not investigated this point further. The lattice parameter correlates also with the guest ion concentration (Figure 5b), monotoni-

dx.doi.org/10.1021/cs4005002 | ACS Catal. 2013, 3, 2256−2268

cally decreasing with an increasing Hf and Zr content. We need to note here, however, that the diffraction peaks of the 20% samples are slightly asymmetric toward higher 2θ, and fitting suggests the presence of a second cubic phase (see the pattern of CeHf-20 in Figure S5 of the Supporting Information). These additional phases can be attributed to c-HfO_2 and c-ZrO_2 doped with Ce, as their lattice parameters are shifted up with respect to the corresponding pure phases. After HCl oxidation, however, no second phase was observed in CeZr-20. Most samples evidence a slight lattice expansion upon HCl oxidation, indicative of an increased level of O vacancy formation (CeO_{2-x} where $x \sim 0.003$) with minor Ce reduction. The cubic phase without disintegration can accommodate much higher vacancy concentrations, even before vacancy ordering starts.[31] The accumulation of vacancies in the bulk of ceria particles during HCl oxidation may occur when nascent surface vacancies are displaced by subsurface oxygen atoms rather than by adsorption from the gas phase.

The contribution of strain, ε_0, to the peak profiles was generally found to be non-negligible but poorly defined, i.e., with comparably large estimated errors. Nevertheless, the overall trend suggests an increase in strain with a higher dopant concentration (Figure S6a of the Supporting Information). This seems plausible from crystal chemistry, as a substitution with differently sized ions should cause local deviations in the d spacings. The crystallite sizes show a slight inverse volcano-type trend but are all found to fall into the same regime of ~10−15 nm (Figure S6b of the Supporting Information). It should be noted that these diffraction-based crystallite sizes cannot be directly compared to the BET surface areas, because the diffracting crystallite domains usually do not represent the primary particles.

Contactless Conductivity Experiments Using the Microwave Cavity Perturbation Technique. Contactless microwave conductivity measurements were performed by applying the microwave cavity perturbation technique to pure CeO_2 and selected samples with a 5% dopant concentration in a fixed-bed flow-through reactor. This way, absolute conductivity values of powder samples under operation conditions are accessible without problems typically arising because of electrode−sample contact resistance in conventional electrical conductivity studies.[41] The results are shown in Figure 6, and the most important data are summarized in Table 2. At room temperature, a very low conductivity in the range of 10^{-9} S/cm was measured for pure CeO_2. After doping, however, much larger conductivities were observed. While the tetravalent dopants Hf and Zr caused an increase to 4×10^{-8} S/cm, the trivalent ions induced an even larger increase to 2×10^{-7} S/cm (La) and 2×10^{-5} S/cm (Sm). When the samples were heated to 623 K, the conductivity improved for all samples as expected for semiconductors. While for pure CeO_2 a value of $\sim 1 \times 10^{-6}$ S/cm was measured, doping with tetravalent ions increased the conductivity to 5×10^{-6} S/cm (Zr) and 2×10^{-5} S/cm (Hf). With trivalent ions, even higher values of 8×10^{-5} S/cm (La) and 3×10^{-4} S/cm (Sm) were obtained. Notably, samples doped with Hf and Zr reached already at around 473 K (Zr) and 533 K (Hf) a rather constant conductivity value, which did not increase further upon the sample being heated to 623 K.

At 623 K, the CeO_2 sample was exposed to air, but no conductivity changes could be recognized. This treatment was followed by an exposure to a gas mixture of 2% H_2 in N_2. Here, an increase in conductivity to 9×10^{-5} S/cm (i.e., an increase of a factor of 90) was determined. Further conductivity rise was still observed after we had switched back to the inert N_2 atmosphere. However, this initial increase turned into a rapidly decreasing conductivity after a few minutes. This effect is due to bulk diffusion processes, e.g., due to migration of oxygen to the surface to compensate for the large number of surface defects. A final treatment in N_2 containing different concentrations of O_2 accelerated the conductivity decrease up to a then constant value of $\sim 1 \times 10^{-6}$ S/cm, which is similar to the conductivity observed during the first measurement cycle in N_2. Similar trends were observed for all investigated doped samples, but with enormous relative differences between trivalent and tetravalent dopants. While for CeO_2 doped with tetravalent ions the conductivity increased in H_2 by more than 3 orders of magnitude (factors of 4000 for Zr and 2000 for Hf), the values increased only slightly for La (factor of 2.5) and Sm (factor of 2.7). Hence, in H_2 and N_2, the conductivity of the tetravalent-doped samples exceeds that of the trivalent-doped samples by up to 2 orders of magnitude.

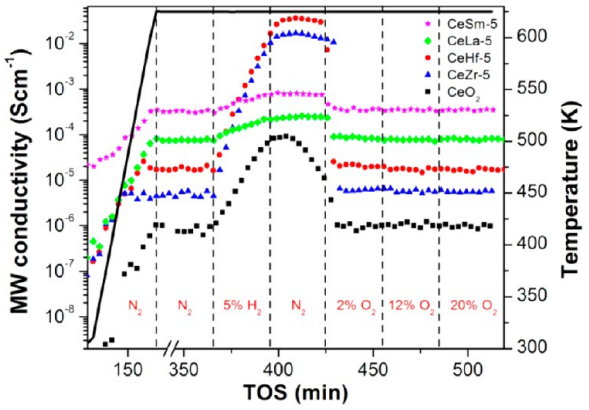

Figure 6. Microwave (MW) conductivity at 9.2 GHz of undoped and doped CeO_2 powder samples in different gas mixtures as indicated, with N_2 as the residual gas. As for CeO_2, between 170 and 350 min time on stream (TOS) the sample was treated in mixtures containing 2−20% O_2 in N_2 (not directly labeled), but no conductivity changes were observed.

Table 2. Steady-State Microwave Conductivity Data for Selected Doped and Undoped CeO_2 Measured under Different Conditions As Shown in Figure 6

sample	E_H (eV)	σ_e(30 °C) (S/cm)	σ_e(350 °C) in N_2 (S/cm)	σ_e(350 °C) in H_2 (S/cm)
CeO_2	0.32	$\approx 10^{-9}$	1×10^{-6}	9×10^{-5}
CeLa-5	0.19	2×10^{-7}	8×10^{-5}	2×10^{-4}
CeSm-5	0.12	2×10^{-5}	3×10^{-4}	8×10^{-4}
CeZr-5	0.14	4×10^{-8}	5×10^{-6}	2×10^{-2}
CeHf-5	0.15	4×10^{-8}	2×10^{-5}	4×10^{-2}

In summary, doping with 5% Zr, Hf, Sm, or La increased the conductivity throughout the whole studied temperature range between 303 and 623 K, with the largest effect measured for trivalent dopants (Sm > La > Hf > Zr). In contrast, the effect of reducing gases, i.e., the difference in conductivity between H_2 and O_2 atmospheres, is largest for tetravalent ions and smallest for trivalent ions (Zr > Hf ≫ La ≈ Sm).

DFT Calculations. As expected, calculations showed that the bulk structure doped with the trivalent cations (La and Sm) gives rise to the expansion of the cubic lattice constant (~0.3 and ~0.1%, respectively), while the samples doped with tetravalent cations Hf and Zr result in its contraction (~0.5

dx.doi.org/10.1021/cs4005002 | ACS Catal. 2013, 3, 2256−2268

and 0.4%, respectively). Thus, the lattice parameters decrease as follows: CeLa > CeSm > Ce > CeZr ≈ CeHf (in line with experiments).

The Deacon process on CeO_2 was described as involving surface oxygen and vacancy sites being able to trap the incoming HCl as OH and Cl (and finally as water; steps D1−D3), the activation of Cl from lattice positions (step D4) with concomitant desorption (step D5), and surface reoxidation (step D6).[12]

$$HCl + O_{\square} + \square \rightarrow O_{\square}H + Cl_{\square} \quad \text{(D1)}$$

$$HCl + O_{\square}H + * \rightarrow H_2O_{\square} + Cl^* \quad \text{(D2)}$$

$$H_2O_{\square} \rightarrow \square + H_2O \quad \text{(D3)}$$

$$Cl_{\square} + Cl^* + * \rightarrow \square + Cl^* + Cl^* \quad \text{(D4)}$$

$$Cl^* + Cl^* \rightarrow Cl_2 + 2^* \quad \text{(D5)}$$

$$\square + \frac{1}{2}O_2 \rightarrow CeO_2 \quad \text{(D6)}$$

where □ denotes an anionic vacant or occupied site and * a Ce on-top site. The catalytic activity of the surface can thus be summarized as its ability to maintain oxygen atoms on the surface and expel Cl atoms from lattice positions; these two descriptors are the oxygen and chlorine vacancy formation. We computed the energy required for these two processes as follows:

$$CeO_2 \rightarrow CeO_{2-x} + \frac{1}{2}O_2 \quad (2)$$

$$CeO_2(Cl_{\square}) \rightarrow CeO_{2-x} + \frac{1}{2}Cl_2 \quad (3)$$

where in the second case the Cl atom is occupying a lattice position, just as oxygen in the first one. For the O and Cl vacancy formation descriptors, we split the contributions according to geometric and electronic factors as both appear when an impurity is present.

To analyze geometric contributions, the vacancy formation energies for oxygen and chlorine lattice atoms were calculated without any dopants but as a function of the lattice constant, within a range of ±10% of the ideal CeO_2, a_{CeO_2}, for the lowest-energy surface, (111) (Figure 7). According to the calculations, the elimination of Cl from the lattice is nearly constant, whereas the removal of O is strongly affected by the contraction and expansion of the lattice (a/a_{CeO_2}). In particular, in the far contracted region (yellow), oxygen is so difficult to remove from the surface that no Cl is available to produce Cl_2. Conversely, in the far expanded region (blue), oxygen is easily removed from the surface and no oxygen is left on the surface to make the reaction evolve. In slightly contracted cells (a/a_{CeO_2} ≈ 0.98), the Cl and O vacancy formation curves cross, and this indicates that at this lattice value the two energies are well balanced.

Electronic effects were analyzed for the (111) and (110) surfaces, now including dopants explicitly. First, the segregation of dopants was investigated (Table 3). On the basis of the segregation energies, in the (111) surface there is almost no preference of the impurity for the surface or subsurface positions, except for La, which prefers to be on the surface. On the other hand, impurities on the (110) surface are slightly favored.

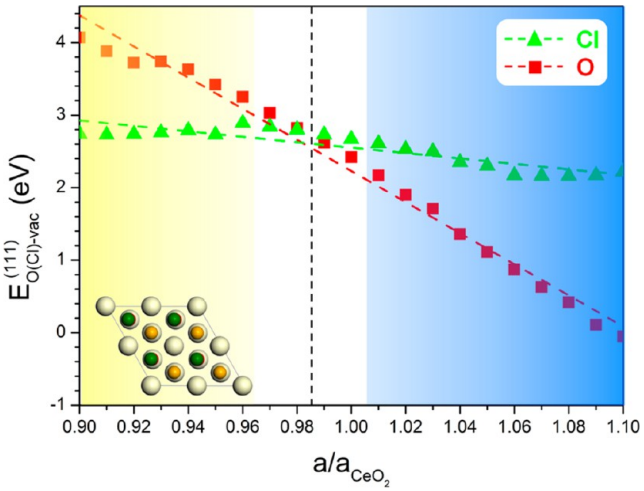

Figure 7. Calculated formation energies for oxygen and chlorine surface defects as a function of *x*- and *y*-lattice expansion in an undoped p(2 × 2) CeO_2 (111) surface.

Table 3. Segregation Energies (E_{seg} in electronvolts) for M-Doped CeO_2 (111) and (110) Surfaces

M	$E_{seg}^{(111)}$	$E_{seg}^{(110)}$
Hf	0.08	−0.10
Zr	0.09	−0.10
La	−0.41	−0.29
Sm	0.00	0.00

Taking the dopant distribution into account, we next calculated the oxygen and chlorine vacancy formation energies for different positions close to and far from the dopant M and for M sitting in the surface or subsurface position [only surface M was considered for (110) surfaces (Figure 8)]. All dopants reduce the energy penalty for forming oxygen and chlorine vacancies. The effect on oxygen vacancy formation is in good agreement with previous results.[22,58,59]

The oxygen vacancy formation energies on the (111) surface are ∼2.4 eV for the native CeO_2, with those of CeHf and CeZr being ∼1.5 eV for the nearest neighbor defect and ∼0.6 eV with the La and Sm impurities. This effect is maintained for next nearest neighbors in the case of La and Sm, in line with previous calculations with lower-valence dopants,[59] and also if the dopant is in the subsurface region. For the open (110) surface, the effect is less pronounced as the reference CeO_2 value is 1.45 eV, with tetravalent cations around 0.7 eV and trivalent cations around ∼0.4 eV.

The effect on the Cl vacancy formation energies is much smoother. The reference value is ∼2.7 eV for the CeO_2(111) surface but it is reduced by almost 1 eV for the tetravalent cations on the surface and by 0.3 eV for trivalent La and Sm. For the (110) surface, the reduction in the vacancy formation energy is smaller than for the compact surface and accounts for 0.4 eV for the tetravalent M cations (in the nearest neighbor position) and 0.3 eV for trivalent cations (in the next nearest neighbor position). Finally, Cl is large enough that it cannot easily penetrate into the lattice, and hence, the surface vacancy formation energies are the relevant cases.

Considering the geometric and electronic contributions described above, it follows that for the trivalent ions there is

dx.doi.org/10.1021/cs4005002 | ACS Catal. 2013, 3, 2256−2268

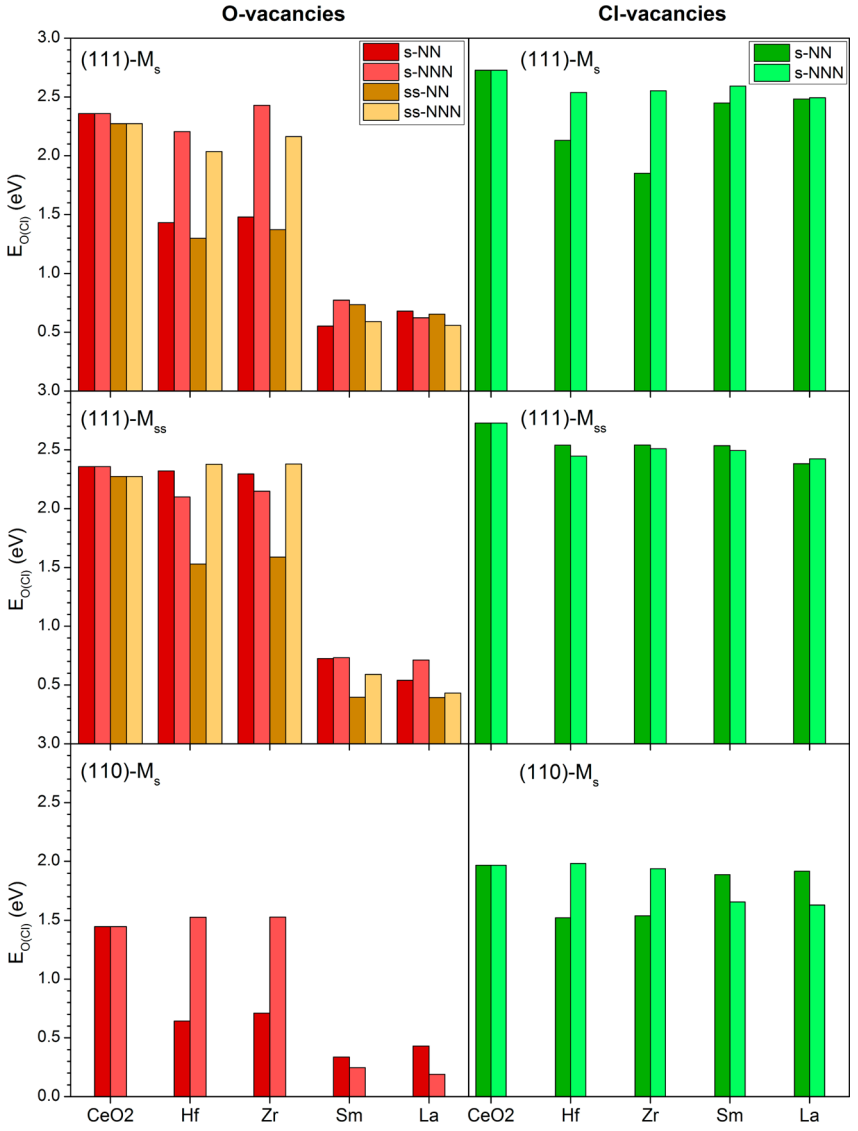

Figure 8. O and Cl vacancy formation energies with respect to gas-phase oxygen or chlorine (E_O or E_{Cl}), for the different undoped CeO_2 and M-doped surfaces. The relative positions of the dopant and the vacancy are indicated as follows: s for surface position, ss for subsurface position, and NN and NNN for the vacancy being the nearest and next nearest neighbor to M, respectively. See Figure 1 for further details.

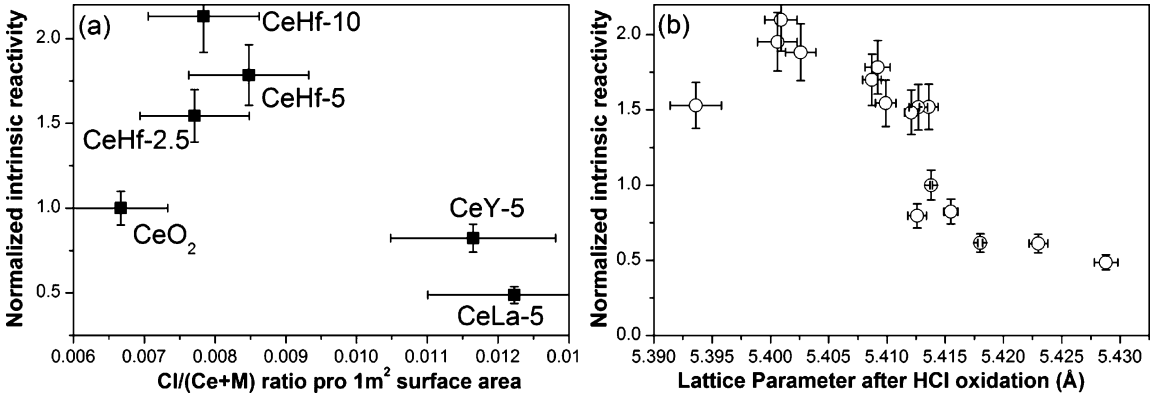

Figure 9. Intrinsic reactivity as a function of (a) the Cl uptake pro surface area as measured by *in situ* PGAA and (b) the lattice parameter after HCl oxidation. The normalized intrinsic reactivity is based on the description provided in the legend of Figure 2b; however, the numbers are scaled to provide CeO_2 an intrinsic reactivity value of 1. Error bars assume for the lattice parameter ±3 times the estimated standard uncertainties and for Cl uptake and normalized intrinsic reactivity ±10% of the actual value. The ±10% error is an estimate of the convoluted error of reactivity + the BET value and the PGAA accuracy + the BET value.

dx.doi.org/10.1021/cs4005002 | *ACS Catal.* 2013, 3, 2256−2268

an extra electronic contribution that makes oxygen vacancy formation less energy-demanding than for tetravalent ions. The reason for this lowest energy requirement for trivalent dopants is the fact that upon forming the defect only one electron is left per oxygen vacancy, and the other is stabilized by the dopant. This means for trivalent cations that there is no significant energy penalty due to electronic repulsion, as is the case for tetravalent cations, where two electrons are located in the vacancy. However, there is also a clear electronic contribution for tetravalent dopants, as the geometric contribution would rather dictate an increase in the oxygen vacancy formation energy. The low O vacancy formation energy in the trivalent systems is not accompanied by a significant decrease in the chlorine energy. This suggests that under HCl oxidation conditions the whole surface of ceria with trivalent dopants is chlorinated, and therefore, reaction D1 cannot take place efficiently.

***In Situ* PGAA.** The chlorine coverage is one decisive parameter of reactivity, and we have conducted *in situ* PGAA experiments to evaluate the surface uptake of Cl under HCl oxidation conditions of selected catalysts. In Figure 9a, the normalized intrinsic reactivity (see the description above) is shown as a function of Cl uptake [expressed as the Cl/(Ce + M) ratio] at 703 K in a 9:1 O_2/HCl reaction mixture. For the sake of convenience, the intrinsic reactivity of 1 corresponds to CeO_2. The experiments indicate the lowest level of Cl uptake for undoped CeO_2, the highest level of uptake for catalysts with trivalent dopants, and a weak volcano-shaped trend. The higher level of chlorination upon trivalent doping is in good agreement with the DFT prediction.

DISCUSSION

Oxidative redox reactions over ceria catalysts require the formation of surface oxygen vacancies, and the creation and transport of vacancies can be effectively modulated by dopants. Because the maximal conductivity and the lowest apparent activation energy of conduction in doped ceria materials are usually reached in the 5−10% dopant concentration range,[60,61] we first prepared 5% doped catalysts and evaluated them in HCl oxidation. Zr and Hf promoted the HCl oxidation reactivity of CeO_2, whereas trivalent dopants (La, Gd, Sm, and Y) were detrimental. Concentration optimization identified 10% Hf- and 10−20% Zr-doped ceria as the best catalysts among the materials tested. The slight deactivation revealed by the stability test fits well to an inverse observation of strongly bound OH buildup (in a similar time frame)[62] that, because of its extended stability, would block a part of the active surface units and thereby act as a deactivating agent. Furthermore, CO oxidation was utilized as a test reaction, and we found that similar to HCl oxidation Hf and Zr dopants enhance the CO oxidation rate, in good agreement with a previous literature report.[35] The best reactivity was observed with CeHf-5, whereas the worst performance (<55% CO conversion) was found with CeSm-5. Doping with La gave no improvement in reactivity below 590 K, which is at odds with an earlier report of La-doped alumina-supported ceria.[34] Because HCl oxidation is severely product-inhibited, the similarities in the two reactions may suggest that CO_2 could also act as an inhibiting agent via strongly bound carbonate species. This would be in line with the observations of Wu et al.[30] showing that the majority of carbonate species are spectators in CO oxidation. This aspect may initiate further studies. Although both reactions require the formation of surface vacancies, the reactivity ordering in the two reactions does not completely follow the same line. We therefore assessed various physicochemical properties of the catalysts to improve our understanding of the requirements of a good ceria-based HCl oxidation catalyst.

In particular, the electronic conductivity was investigated using a microwave cavity perturbation technique at 623 K, slightly above the temperature of the onset of HCl oxidation and in the temperature regime of CO oxidation. Under inert or oxidizing conditions, dopants give rise to a much enhanced conductivity compared to that of CeO_2, the trivalent dopants being the most effective. On the contrary, under reducing conditions Hf and Zr promote very high conductivity, whereas trivalent-doped materials exhibit only minor modulation. This dependence of electronic conductivity on reaction conditions can be rationalized in terms of the number of mobile charge carriers under certain conditions (*vide infra*).

It is generally accepted that electron transport in the n-type semiconductor ceria can be described by a small polaron transport process, i.e., by a thermally activated hopping mechanism.[31,63,64] Under reducing conditions, ceria tends to lose oxygen to the ambient atmosphere, accompanied by the creation of oxygen vacancies and a change in the oxidation state from +4 to +3 of an adjacent cerium ion. This can be written using the Kröger−Vink notation as

$$O_O^x + H_2 + 2Ce_{Ce}^x \rightarrow H_2O + V_O^{\cdot\cdot} + 2Ce_{Ce}' \quad (4)$$

where O_O^x represents an oxygen lattice site (i.e., O^{2-}), Ce_{Ce}^x is a normal cerium atom in a cerium site (i.e., Ce^{4+}), $V_O^{\cdot\cdot}$ is a doubly positively charged vacancy in an oxygen site, and Ce_{Ce}' is a single negatively charged cerium (i.e., Ce^{3+}) in a cerium site.

Hence, electronic conductivity σ_e can be expressed as

$$\sigma_e = [Ce_{Ce}']e\mu \quad (5)$$

where $[Ce_{Ce}']$ is the concentration of charge carriers (located at a Ce atom), e is the elementary charge, and μ is the mobility defined by

$$\mu = \frac{A}{T}\exp\left(\frac{-E_H}{k_B T}\right) \quad (6)$$

where A is a constant (further described in ref 63), E_H is the activation energy for the electron hopping process, and k_B is Boltzmann's constant.

Hence, by plotting $\log(\sigma_e T)$ versus the reciprocal temperature $(1/T)$, we determined the hopping transport activation energies for all studied samples (see Figure S2 of the Supporting Information as an example). As a result, a value of 0.32 eV was obtained for the pure CeO_2 sample. This value is well in the range of 0.4 eV found by Mogensen et al.[31] and 0.2 eV measured by Naik and Tien[64] for nearly stoichiometric CeO_2. This rather low activation energy furthermore indicates that with the microwave technique electronic conduction is measured rather than ionic charge transport, the latter having typical activation energies of $\gtrsim$0.7 eV. In such cases, ionic mobility measures not only vacancy hopping but also vacancy formation (or association with dopants).[31,65,66] From the computational point of view, the difference in energy between charge distributions that can be linked to the electronic mobility is found to be 0.27 eV. This is the difference in energy between two identical structures where the electrons are either close to or far from the vacancy site (E_{pol} in Table S1 of the Supporting Information). This is in agreement with previously reported values.[18] Moreover, the mobility of oxygen vacancies

dx.doi.org/10.1021/cs4005002 | ACS Catal. 2013, 3, 2256−2268

implies also the redistribution of charge in nearby Ce atoms, thus inducing charge mobility. Oxygen vacancy hopping shows a diffusion barrier with a concomitant charge redistribution of 0.34 eV.

The presence of trivalent dopants affects the initial number of carriers, assuming a single phase, as follows:

$$M^{3+} + CeO_2 \rightarrow (MCe')_{Ce}CeO_2 \quad (7)$$

Therefore, in inert or oxidizing atmospheres, the doping reaction (eq 7) controls the numbers of carriers. Indeed, experiments show that the conductivity decreases in the following order: trivalent > tetravalent > CeO_2.

Under reducing conditions, oxygen vacancy generation plays an important role, and thus, both eqs 4 and 7 should be taken into account. Under heavy reduction conditions, eq 4 will be the dominating term as reduction is eased for all samples. Upon vacancy formation, tetravalent dopants generate twice the number of charge carriers as trivalent ions; thus, the electronic conductivity shall be larger for M^{4+}.

Compared to that of pure ceria, significantly lower activation energies were determined for the doped ceria samples in the microwave conductivity experiment, with 0.15 eV for Hf, 0.14 eV for Zr, 0.19 eV for La, and 0.12 eV for Sm. In this case, the computed differences between the charge distributions (associated with a moving polaron) are between 0.09 eV for La and 0.17 eV for Hf. For a homogeneous distribution of vacancies, vacancy hopping with electron redistribution implies also low barriers of ∼0.14 and ∼0.22 eV for Hf and La, respectively. More details about these calculations are given in Figure S7 and Table S1 of the Supporting Information.

Comparing the HCl oxidation results with the O vacancy formation energy and the electronic conductivity under inert and oxidizing conditions, it becomes clear that these properties do not at all correlate with reactivity. It is intriguing that the vacancy formation energy of the catalysts is not followed in CO oxidation either. On the other hand, reducing conditions increase the electronic conductivity of CeZr-5 and CeHf-5, which are indeed better catalysts. Also, the lattice parameter seems to qualitatively follow the reactivity in HCl oxidation, lattice contraction being beneficial and expansion detrimental. To quantitatively visualize the effect of the lattice parameter, we compared the normalized intrinsic reactivity of all samples and plotted them as a function of the lattice parameter determined after reaction. This is shown in Figure 9b, where again the intrinsic reactivity of 1 corresponds to CeO_2. There is a weak trend of decreasing lattice parameter providing better reactivity, and the effect peaks near 5.4 Å (CeHf-10, CeZr-10, and CeZr-20). Greater lattice contraction does not seem to be advantageous, though we need to keep in mind that CeHf-20 was biphasic. The fact that the most efficient support for ceria was found to be ZrO_2[13] is not surprising, considering that nanoclusters of ceria on the ZrO_2 carrier could be compressively strained or part of Zr might be incorporated into the ceria clusters. Because HCl oxidation is a surface process, it is not per se evident why a bulk property (lattice parameter) should directly correlate with the catalytic rate. Nevertheless, one might envisage that the strained lattice extends onto the surface, giving rise to a modified adsorption strength.

With regard to the effect of surface coverage with chlorine, *in situ* PGAA indicated that intermediate coverages give rise to better reactivity. Although in our previous work[38] we concluded that most of the Cl uptake was related to the part of the surface that is not relevant for HCl oxidation, nevertheless, the trends of Cl uptake observed as a function of experimental parameters (T and partial pressure of reactants) were thought to be still valid for the small portion of the surface responsible for the catalytic reaction. Likewise, the Cl uptake of this experiment traces the overall surface, mostly not directly involved in HCl oxidation, but the volcano-type Cl uptake may still be relevant and could suggest that an intermediate Cl coverage of the active surface units could give rise to the largest reactivity. The comparison of Cl and O vacancy formation energies suggests that the highest activity shall be observed for the systems with the concomitant reduction of the vacancy formation energies for Cl and O. This is most effectively achieved for tetravalent ions. In comparison, trivalent ions are very effective at forming oxygen vacancies, but this ends up with the chlorination of the surface. Additionally, Hu and Metiu[67] have shown that doping ceria with trivalent La gives rise to a stabilization of on-top Cl adsorption (one Cl on Ce and another Cl on O) because of a strong interaction between the Lewis acid and Lewis base Cl atoms in Cl−Ce and Cl−O bonds, respectively. Such stabilization is admittedly not beneficial for desorbing Cl_2 from the surface and will hinder reactivity.

Studt et al.[68] using DFT calculations evaluated various rutile oxide surfaces in HCl oxidation and found that the dissociative adsorption energy of O_2 is a good descriptor of the reactivity. Recently, Over and Schomäcker[69] compiled experimental reactivity data and suggested a similar volcano dependence as a function of the same descriptor. In general, dissociation of molecules on surfaces is thought to be strongly structure sensitive because of the productlike late nature of the transition state.[70] Although no O_2 adsorption occurred at 173 K on nanocrystals of ceria with controlled morphology (octahedra, cubes, and rods) after calcination, the O_2 chemisorption was structure sensitive on the prereduced nanocrystals.[27] Therefore, our observation[38] that only a small portion of the surface is responsible for the reactivity (structure or defect sensitivity) is overall in line with the predictions of the descriptor. The dissociative adsorption of oxygen can be seen as the inverse process of O vacancy formation, and therefore, the oxygen adsorption energy is a strong function of dopants. Nevertheless, one needs to be aware that the strong variation of the vacancy formation energy is not compatible with the much less pronounced effect in reactivity.

In summary, there are other parameters (shape of the doped catalyst, surface concentration of dopants, etc.) not considered here that might also play an important role in HCl oxidation; nevertheless, our observations suggest that lattice contraction using dopants with smaller ionic radii is beneficial. Clearly, the reduced O vacancy formation energy alone does not guarantee a good catalyst, and only the balanced reduction of both Cl and O vacancy formation energy allows for an enhanced reactivity.

CONCLUSIONS

We have studied the role of trivalent and tetravalent promotion on the structural, electronic, and catalytic properties of ceria. In particular, our interest was to improve the reactivity of ceria in HCl oxidation. This can be effectively achieved upon promotion with 10% Hf and 10−20% Zr; on the other hand, trivalent dopants are clearly detrimental. There is a weak trend of a decreasing lattice parameter of the cubic structure providing better reactivity, the effect peaking near 5.4 Å, whereas lattice expansion upon trivalent doping is undesirable. We find also a weak volcano behavior between the surface Cl

dx.doi.org/10.1021/cs4005002 | ACS Catal. 2013, 3, 2256−2268

coverage and the reactivity, indicating that intermediate Cl coverages are preferred. Although both HCl oxidation and CO oxidation rely on the existence of oxygen vacancies, the orders of reactivity in these reactions are not completely identical, suggesting that CO oxidation might not always be appropriate as a test reaction for other redox reactions. The oxygen vacancy formation energy and the electronic conductivity of promoted catalysts were assessed under inert or oxidizing conditions, and neither of these properties correlates with the reactivity in HCl oxidation. DFT calculations indicate that only the balanced reduction of both Cl and O vacancy formation energy allows for an enhanced reactivity.

■ ASSOCIATED CONTENT

Supporting Information

Details of *in situ* PGAA, microwave conductivity setup, additional HCl oxidation results, additional CO oxidation results, X-ray diffraction strain and size analysis, and additional DFT results. This material is available free of charge via the Internet at http://pubs.acs.org.

■ AUTHOR INFORMATION

Corresponding Author

*E-mail: teschner@fhi-berlin.mpg.de.

Notes

The authors declare no competing financial interest.

■ ACKNOWLEDGMENTS

We thank ERC-StG'10, MINECO for support through Project CTQ2012-33826/BQU and BSC-RES for generously providing computational resources. We thank Patrick Kast for allowing us to use his reactor setup for CO oxidation.

■ REFERENCES

(1) Khartona, V. V.; Marquesa, F. M. B.; Atkinson, A. *Solid State Ionics* **2004**, *174*, 135−149.
(2) Fergus, J. W. *J. Power Sources* **2006**, *162*, 30−40.
(3) Trovarelli, A. *Catal. Rev.: Sci. Eng.* **1996**, *38*, 439−520.
(4) Yoo, J. S.; Bhattacharyya, A. A.; Radlowski, C. A.; Karch, J. A. *Appl. Catal., B* **1992**, *1*, 169−189.
(5) Yoo, J. S.; Bhattacharyya, A. A.; Radlowski, C. A. *Ind. Eng. Chem. Res.* **1991**, *30*, 1444−1448.
(6) Aneggi, E.; de Leitenburg, C.; Llorca, J.; Trovarelli, A. *Catal. Today* **2012**, *197*, 119−126.
(7) Fu, Q.; Saltsburg, H.; Flytzani-Stephanopoulos, M. *Science* **2003**, *301*, 935−938.
(8) Hilaire, S.; Wang, X.; Luo, T.; Gorte, R. J.; Wagner, J. *Appl. Catal., A* **2001**, *215*, 271−278.
(9) Schubert, M. M.; Plzak, V.; Garche, J.; Behm, R. J. *Catal. Lett.* **2001**, *76*, 143−150.
(10) Pozdnyakova, O.; Teschner, D.; Wootsch, A.; Kröhnert, J.; Steinhauer, B.; Sauer, H.; Toth, L.; Jentoft, F. C.; Knop-Gericke, A.; Paál, Z.; Schlögl, R. *J. Catal.* **2006**, *237*, 1−16.
(11) He, J.; Xu, T.; Wang, Z.; Zhang, Q.; Deng, W.; Wang, Y. *Angew. Chem., Int. Ed.* **2012**, *51*, 2438−2442.
(12) Amrute, A. P.; Mondelli, C.; Moser, M.; Novell-Leruth, G.; López, N.; Rosenthal, D.; Farra, R.; Schuster, M. E.; Teschner, D.; Schmidt, T.; Pérez-Ramírez, J. *J. Catal.* **2012**, *286*, 287−297.
(13) Moser, M.; Mondelli, C.; Schmidt, T.; Girgsdies, F.; Schuster, M. E.; Farra, R.; Szentmiklósi, L.; Teschner, D.; Pérez-Ramírez, J. *Appl. Catal., B* **2013**, *132*, 123−131.
(14) Esch, F.; Fabris, S.; Zhou, L.; Montini, T.; Africh, C.; Fornasiero, P.; Comelli, G.; Rosei, R. *Science* **2005**, *309*, 752−755.
(15) Sayle, T. X. T.; Parker, S. C.; Catlow, C. R. A. *Surf. Sci.* **1994**, *316*, 329−336.
(16) Fabris, S.; Vicario, G.; Balducci, G.; de Gironcoli, S.; Baroni, S. *J. Phys. Chem. B* **2005**, *109*, 22860−22867.
(17) Nolan, M.; Parker, S. C.; Watson, G. W. *Surf. Sci.* **2005**, *595*, 223−232.
(18) Ganduglia-Pirovano, M. V.; Da Silva, J. L. F.; Sauer, J. *Phys. Rev. Lett.* **2009**, *102*, 026101.
(19) Jerratsch, J.-F.; Shao, X.; Nilius, N.; Freund, H.-J.; Popa, C.; Ganduglia-Pirovano, M. V.; Burow, A. M.; Sauer, J. *Phys. Rev. Lett.* **2011**, *106*, 246801.
(20) Murgida, G. E.; Ganduglia-Pirovano, M. V. *Phys. Rev. Lett.* **2013**, *110*, 246101.
(21) Krcha, M. D.; Mayernick, A. D.; Janik, M. J. *J. Catal.* **2012**, *293*, 103−115.
(22) Nolan, M. *J. Phys. Chem. C* **2009**, *113*, 2425−2432.
(23) Nolan, M.; Parker, S. C.; Watson, G. *Phys. Chem. Chem. Phys.* **2006**, *8*, 216−218.
(24) Yeriskin, I.; Nolan, M. *J. Phys.: Condens. Matter* **2010**, *22*, 1350041-8.
(25) Nolan, M. *J. Phys. Chem. C* **2011**, *115*, 6671−6681.
(26) Aryanpour, M.; Khetan, A.; Pitsch, H. *ACS Catal.* **2013**, *3*, 1253−1262.
(27) Wu, Z.; Li, M.; Howe, J.; Meyer, H. M.; Overbury, S. H. *Langmuir* **2010**, *26*, 16595−16606.
(28) Aneggi, E.; Llorca, J.; Boaro, M.; Trovarelli, A. *J. Catal.* **2005**, *234*, 88−95.
(29) Zhou, K.; Wang, X.; Sun, X.; Peng, Q.; Li, Y. *J. Catal.* **2005**, *229*, 206−212.
(30) Wu, Z.; Li, M.; Overbury, S. H. *J. Catal.* **2012**, *285*, 61−73.
(31) Mogensen, M.; Sammes, N. M.; Tompsett, G. A. *Solid State Ionics* **2000**, *129*, 63−94.
(32) Fally, F.; Perrichon, V.; Vidal, H.; Kaspar, J.; Blanco, G.; Pintado, J. M.; Bernal, S.; Colon, G.; Daturi, M.; Lavalley, J. C *Catal. Today* **2000**, *59*, 373−386.
(33) Putna, E. S.; Bunluesin, T.; Fan, X. L.; Gorte, R. J.; Vohs, J. M.; Lakis, R. E.; Egami, T. *Catal. Today* **1999**, *50*, 343−352.
(34) Katta, L.; Thrimurthulu, G.; Reddy, B. M.; Muhler, M.; Grünert, W. *Catal. Sci. Technol.* **2011**, *1*, 1645−1652.
(35) Reddy, B. M.; Bharali, P.; Saikia, P.; Khan, A.; Loridant, S.; Muhler, M.; Grünert, W. *J. Phys. Chem. C* **2007**, *111*, 1878−1881.
(36) Kalamaras, C. M.; Dionysiou, D. D.; Efstathiou, A. M. *ACS Catal.* **2012**, *2*, 2729−2742.
(37) Kalamaras, C. M.; Petallidou, K. C.; Dionysiou, D. D.; Efstathiou, A. M. *Appl. Catal., B* **2013**, *136−137*, 225−238.
(38) Farra, R.; Eichelbaum, M.; Schlögl, R.; Szentmiklósi, L.; Schmidt, T.; Amrute, A. P.; Mondelli, C.; Pérez-Ramírez, J.; Teschner, D. *J. Catal.* **2013**, *297*, 119−127.
(39) *TOPAS*, version 4.2; Bruker AXS, 2009.
(40) Balzar, D. In *Microstructure Analysis from Diffraction*; Snyder, R. L., Bunge, H. J., Fiala, J., Eds.; International Union of Crystallography: Chester, U.K., 1999.
(41) Eichelbaum, M.; Stößer, R.; Karpov, A.; Dobner, C.-K.; Rosowski, F.; Trunschke, A.; Schlögl, R. *Phys. Chem. Chem. Phys.* **2012**, *14*, 1302−1312.
(42) Kresse, G.; Furthmüller, J. *Comput. Mater. Sci.* **1996**, *6*, 15−50.
(43) Kresse, G.; Furthmüller, J. *Phys. Rev. B* **1996**, *54*, 11169−11186.
(44) Perdew, J.; Burke, K.; Ernzerhof, M. *Phys. Rev. Lett.* **1996**, *77*, 3865−3868.
(45) Dudarev, S. L.; Botton, G. A.; Savrasov, S. Y.; Humphreys, C. J.; Sutton, A. P. *Phys. Rev. B* **1998**, *57*, 1505−1509.
(46) Fernández-Torre, D.; Kośmider, K.; Carrasco, J.; Ganduglia-Pirovano, M. V.; Pérez, R. *J. Phys. Chem. C* **2012**, *116*, 13584−13593.
(47) Blöchl, P. E. *Phys. Rev. B* **1994**, *50*, 17953−17979.
(48) Monkhorst, H. J.; Pack, J. D. *Phys. Rev. B* **1976**, *13*, 5188−5192.
(49) Da Silva, J. L. F.; Ganduglia-Pirovano, M. V.; Sauer, J.; Bayer, V.; Kresse, G. *Phys. Rev. B* **2007**, *75*, 045121.
(50) For consistency, the same localization of the excess of charge was imposed in all the spin-polarized calculations. See the Supporting Information for details.

(51) Andersson, D. A.; Simak, S. I.; Johansson, B.; Abrikosov, I. A.; Skorodumova, N. V. *Phys. Rev. B* **2007**, *75*, 035109.
(52) Paier, J.; Penschke, C.; Sauer, J. *Chem. Rev.* **2013**, *113*, 3949−3985.
(53) Constable, F. H. *Proc. R. Soc. London, Ser. A* **1925**, *108*, 355−378.
(54) Cremer, E. *Adv. Catal.* **1955**, *7*, 75−91.
(55) Teschner, D.; Novell-Leruth, G.; Farra, R.; Knop-Gericke, A.; Schlögl, R.; Szentmiklósi, L.; Hevia, M. G.; Soerijanto, H.; Schomäcker, R.; Pérez-Ramírez, J.; López, N. *Nat. Chem.* **2012**, *4*, 739−745.
(56) Teschner, D.; Farra, R.; Yao, L.; Schlögl, R.; Soerijanto, H.; Schomäcker, R.; Schmidt, T.; Szentmiklósi, L.; Amrute, A. P.; Mondelli, C.; Pérez-Ramírez, J.; Novell-Leruth, G.; López, N. *J. Catal.* **2012**, *285*, 273−284.
(57) In a flow reactor, assuming small changes in the concentration of educts between bed segments, a doubled conversion and thus doubled product concentration will cut the reaction rate in half, and as both products inhibit the reaction by −1 order, the rate decreases by a factor of 2 × 2 = 4. That is, 4 times the weight provides twice the conversion, and thus, we obtain the 0.5 order dependence on catalyst weight. Fitting the actual data points in the 0−53% conversion range suggests an order of 0.505, in very good agreement with the prediction.
(58) Andersson, D. A.; Simak, S. I.; Skorodumova, N. V.; Abrikosov, I. A.; Johansson, B. *Appl. Phys. Lett.* **2007**, *90*, 031909.
(59) Hu, Z.; Metiu, H. *J. Phys. Chem. C* **2011**, *115*, 17898−17909.
(60) Faber, J.; Geoffroy, C.; Roux, A.; Sylvestre, A.; Abélard, P. *Appl. Phys. A: Mater. Sci. Process.* **1989**, *49*, 225−232.
(61) Inaba, H.; Tagawa, H. *Solid State Ionics* **1996**, *83*, 1−16.
(62) Farra, R.; Schuster, M. E.; Wrabetz, S.; Stotz, E.; Hamilton, N. G.; Amrute, A. P.; Pérez-Ramírez, J.; López, N.; Teschner, D. *Phys. Chem. Chem. Phys.* **2013**, *15*, 3454−3465.
(63) Tuller, H. L.; Nowick, A. S. *J. Phys. Chem. Solids* **1977**, *38*, 859−867.
(64) Naik, I. K.; Tien, T. Y. *J. Phys. Chem. Solids* **1978**, *39*, 311−315.
(65) Andersson, D. A.; Simak, S. I.; Skorodumova, N. V.; Abrikosov, I. A.; Johansson, B. *Proc. Natl. Acad. Sci. U.S.A.* **2006**, *103*, 3518−3521.
(66) Shoko, E.; Smith, N. F.; McKenzie, R. H. *J. Phys. Chem. Solids* **2011**, *72*, 1482−1494.
(67) Hu, Z.; Metiu, H. *J. Phys. Chem. C* **2012**, *116*, 6664−6671.
(68) Studt, F.; Abild-Pedersen, F.; Hansen, H. A.; Man, I. C.; Rossmeisl, J.; Bligaard, T. *ChemCatChem* **2010**, *2*, 98−102.
(69) Over, H.; Schomäcker, R. *ACS Catal.* **2013**, *3*, 1034−1046.
(70) van Santen, R. A.; Neurock, M.; Shetty, S. G. *Chem. Rev.* **2010**, *110*, 2005−2048.
(71) Shannon, R. D. *Acta Crystallogr.* **1976**, *A32*, 751−767.